Spatial variations in luminescence and carrier relaxation in molecular beam epitaxial grown $(InP)_2/(GaP)_2$ quantum wires

Y. Tang and D. H. Rich[a)]
Department of Materials Science and Engineering, Photonic Materials and Devices Laboratory, University of Southern California, Los Angeles, California 90089-0241

A. M. Moy and K. Y. Cheng
Department of Electrical and Computer Engineering, Center for Compound Semiconductors Microelectronics, University of Illinois at Urbana-Champaign, Urbana, Illinois 61801

(Received 14 January 1997; accepted 16 April 1997)

Phase separation in III–V semiconductors has led to a unique method for fabricating quantum wires via a strain induced lateral ordering process. Quantum wire (QWR) arrays were formed during the gas source molecular beam epitaxial (MBE) growth of $(InP)_2/(GaP)_2$ bilayer superlattices (BSLs) and were studied by time-resolved and linearly polarized cathodoluminescence. Nonlinear optical properties, such as phase-space filling effects, were observed to be indicative of the QWR nature of the samples. Samples prepared by gas source MBE were found to have a greater uniformity, smaller QWRs, and higher optical quality in comparison to those obtained by metal–organic chemical vapor deposition. Misfit dislocations also formed in one of the BSL samples, indicating a partial strain relaxation at the GaAs/InGaP and BSL/InGaP interfaces. The carrier relaxation, transport, and collection in the QWRs were studied with time-resolved cathodoluminescence. © *1997 American Vacuum Society.* [S0734-211X(97)07504-5]

I. INTRODUCTION

The majority of III–V alloys exhibit miscibility gaps at low temperature and this can result in a lateral phase separation in epitaxial layers as described by spinodal decomposition.[1–8] Phase separation in III–V ternary alloys can occur when local variations in cation concentrations and strain favor "up-hill" diffusion as a means of lowering the free energy of the alloy. The growth of short period strained superlattices likewise creates more interfaces, which enhance the number of cations diffusing laterally and further facilitates phase separation. This strain induced lateral ordering (SILO) method has been utilized to form quantum wire (QWR) arrays in bilayer superlattices (BSLs) of $(InP)_2/(GaP)_2$ and $(GaAs)_2/(InAs)_2$ grown on a GaAs(001) or InP(001) substrate, respectively.[9–14] The optical properties of the QWR structures have been studied with photoluminescence (PL),[9,10] photoreflectance (PR),[11] and cathodoluminescence (CL)[12–14] techniques. A large polarization anistropy was found to be consistent with the existence of QWRs.[9,13] It is of paramount importance to study the optical properties of SILO QWRs in order to understand the interplay between the microstructure, local optical properties, and growth conditions. These QWRs further exhibit good potential for applications in optoelectronics such as for light-emitting diodes, high-speed optical switches, and low-threshold, high-gain QWR lasers.[10,15]

In a previous study, we used CL techniques to examine the nonlinear optical properties of $(InP)_2/(GaP)_2$ BSLs on GaAs(001) substrates grown by metal–organic chemical vapor deposition (MOCVD).[12–14] The combination of linearly polarized CL spectroscopy, CL imaging and time-resolved CL enabled a study of the nonlinear optical properties and carrier relaxation kinetics in the QWR structure.[12–14] In this study, using these CL techniques, we examine the optical and structural properties in the QWR structures grown by gas source molecular beam epitaxy (MBE). Based on the observed optical and structural properties, we show that MBE enables a good control of the growth of short period superlattices used to produce QWR arrays. The spatial homogeneity of the QWR structures was studied with CL imaging and a depth dependent CL study. Misfit dislocations and spot defects were observed in the CL imaging. The QWR luminescence exhibits multiple components; their origin and carrier relaxation into regions giving rise to these components are studied with time-resolved CL.

II. EXPERIMENTAL DETAILS

A schematic diagram of the sample structure is shown in Fig. 1. BSLs of $(InP)_2/(GaP)_2$ were grown on a 3000 Å thick $In_{0.49}Ga_{0.51}P$ buffer layer, which is lattice matched to the underlying GaAs(001) substrate. Details of the gas source MBE system and the BSL growth procedures have been previously reported.[6,9,10] Two samples were grown for this study and labeled as 2067 and 2339, respectively. Each sample consists of four $(InP)_2/(GaP)_2$ BSL regions, each separated by 180-Å-thick $In_{0.49}Ga_{0.51}P$ barriers and is capped with a 300-Å-thick AlInP layer. Each of the four $(InP)_2/(GaP)_2$ BSL regions are ~147 and ~102 Å thick for samples 2067 and 2339, respectively. The rate of the BSL growths was ~1 ML/s. The lateral composition modulation in the bilayer structure occurred during the gas source MBE growth, and the modulation direction is along the [110] direction. The composition of In varies from ~0.33 in the Ga-rich region to ~0.67 in the In-rich region, with periods of

a)Author to whom correspondence should be addressed; Electronic mail: danrich@almaak.usc.edu

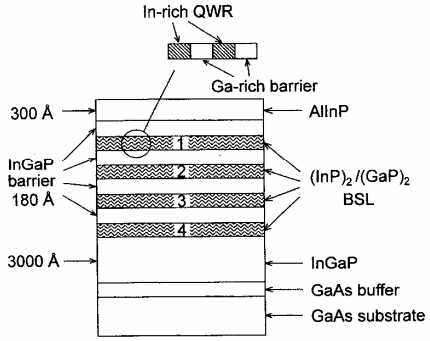

FIG. 1. Schematic diagram of $(InP)_2/(GaP)_2$ bilayer superlattice structure.

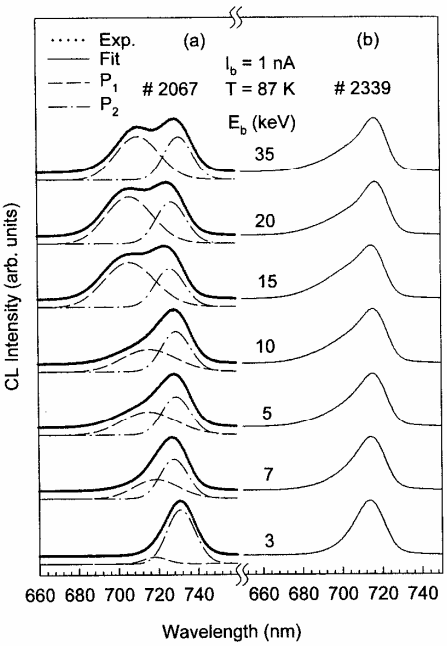

FIG. 2. Stack plots of CL spectra taken with E_b varying from 3 to 35 keV for samples 2067 (a) and 2339 (b). In (a), spectra are fitted with a sum of two Gaussian functions. Solid lines show the fitting results with the decomposed P_1 (dotted lines) and P_2 (dash lines) components offset below each spectrum.

~125 and ~100 Å for sample 2067 and 2339, respectively.[9] Therefore, quantum wire arrays were formed with cross-sectional areas of ~147 Å ×63 Å and ~102 Å ×50 Å with a two-dimensional (2D) quantum confinement in the growth and lateral ordering directions.

The CL experiments were performed with a modified JEOL-840A scanning electron microscope with polarization detection capability described previously.[12–14] In polarization measurements, light with electric-field **E** parallel to the [110] or [1$\bar{1}$0] was detected. The luminescence signal from the sample, whose temperature was maintained at ~87 K by a liquid-nitrogen cryogenic specimen stage, was dispersed by a 1/4 m monochromator and detected by a cooled GaAs:Cs photomultiplier tube with a spectral resolution of ~1 nm. In time-resolved experiments, the method of delayed coincidence in an inverted single photon counting mode was used.[16] Electron-beam pulses of 50 ns width with a 1 MHz repetition rate were used to excite the samples. This enabled the measurement of time-delayed CL spectra with a temporal resolution of ~100 ps. The e-beam energy, E_b, was varied systematically from 3 to 35 keV in the experiments to obtained a tunable electron range and probe depth.

III. RESULTS AND DISCUSSION

A. Excitation-dependent CL spectra

CL spectra of both samples are shown in Fig. 2. The broad peaks located in the $680 \lesssim \lambda \lesssim 750$ nm range are due to emission from the QWR array.[9–14] The CL spectral line shapes are observed to vary with beam energy, particularly for sample 2067, which shows a marked enhancement in the high-energy side of the line shape for higher beam energies. Spectra taken at $E_b = 3$ keV, for both samples, show a line shape very similar to that of PL obtained with an argon–ion laser (not shown here). The polarization anistropy of the integrated CL intensity over the $680 \lesssim \lambda \lesssim 750$ nm range were measured, and $I_\parallel/I_\perp \approx 3$, where $I_\parallel$ and $I_\perp$ are the integrated CL intensities taken with the polarizer orientated so that the electric-field **E** of the detected light is parallel and perpendicular to the quantum wire, respectively. This polarization ratio is about twice as large as compared to samples grown by MOCVD ($I_\parallel/I_\perp \approx 1.5$).[12,13] This may be due to a higher degree of ordering and narrower QWR thickness in the MBE-grown structures, whose compositional modulation period (~100 Å) is much shorter than that observed for the MOCVD-grown structures (~800 Å).[12–14] The substrate temperature for the MOCVD[12] and MBE[6] growths were maintained at ~650 and ~500 °C, respectively. Owing to the temperature difference between the MBE and MOCVD growth, we should, therefore, expect differences accordingly in the composition and spatial wavelength of the resultant QWR regions.[6]

The e-beam probing depth dependence of the CL spectra was studied and a stack plot of CL spectra taken under electron-beam energies E_b ranging from 3 to 35 keV is shown in Fig. 2. We found that in sample 2067 a higher energy luminescence feature emerged for $E_b \geq 10$ keV, and its intensity increased as the electron penetration depth increased. A smaller increase in the CL intensity from the high-energy side of the line shape is observed for sample 2339 in Fig. 2 as the E_b increases. A probe current dependence experiment showed that for a fixed $E_b = 5$ keV, no significant change in the CL spectra line shape occurred in both samples as the probe current increases from 50 pA to 5 nA. Thus, the appearance of these high-energy peaks cannot be attributed directly to an enhanced excitation density and band filling for higher e-beam energies. The two luminescence features evidently arise from separate regions at different depths of the sample. Likewise, in a previous CL

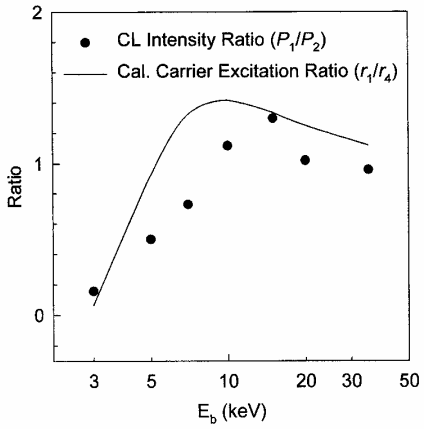

FIG. 3. Intensity ratio of P_1 and P_2 components (filled symbols) and ratio of the calculated carrier excitation rate, r_1/r_4, in the first and fourth BSL layers (solid line) as a function of beam energy.

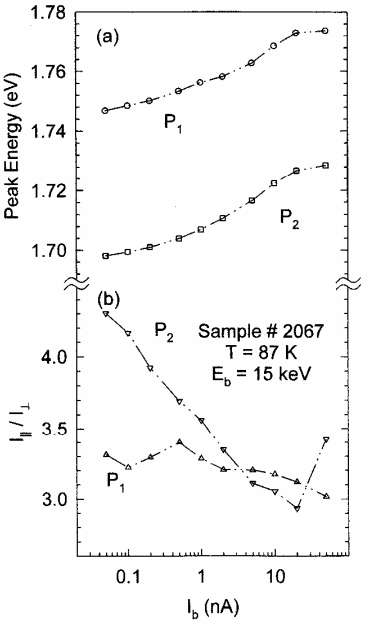

FIG. 4. Peak energy E_p (a) and polarization ratio $I_\parallel/I_\perp$ (b) as a function of probe current for luminescence components P_1 and P_2 for sample 2067.

study, we observed the presence of two or more components in the QWR emission and suggested that they arise from two different QWR widths and/or In compositions.[14] To further quantify the behavior of the CL spectra, we have decomposed the CL line shapes of sample 2067 into the sum of two Gaussian peaks, P_1 and P_2. The fitting results (solid line) are shown in Fig. 2(a) with the two components offset below. The intensity ratio of P_1 and P_2 is shown as a function of beam energy in Fig. 3. For comparison, we show the ratio of the calculated $e-h$ excitation rates, r_i, between QWR regions 1 and 4 (i.e., r_1/r_4, solid line in Fig. 3). We have used a simple one-dimensional depth–dose $e-h$ pair creation function, ignoring carrier diffusion, in this calculation.[17] While a lateral diffusion length of ~ 0.5 μm is typical for the InGaP material system,[18] the effective diffusion length along the growth direction will be reduced as a result of the BSL regions impeding vertical carrier transport. Similar effects have been observed in the related InGaAs/GaAs multiple quantum well system.[19]

It is, thus, reasonable to conclude that P_1 and P_2 originate from the inner (deeper) and outer (shallower) QWR regions, respectively. It is likely that variations in the lateral QWR width and/or In composition modulation occurred during the SILO process. Previous cross-sectional transmission electron microscopy results have shown that the vertical and lateral dimensions of the QWR depend on the location in the BSL region and total film thickness.[6,9] The inner BSL layers have a narrower lateral QWR than that of the outer BSL layers, owing to a strain accumulation effect during growth, which results in a layer-dependent bulk diffusion and phase separation.[6,9] The presence of misfit dislocations (see Sec. III C) indicates the buildup of a net global strain and subsequent strain relaxation during the latter stages of the growth.

Using a transfer matrix method to calculate the ground state excitonic transition energies in the QWRs,[13] we estimate that the P_1 and P_2 energy difference of 47 meV results in a maximum In composition variation of $\sim 6\%$ for a fixed QWR size. For a fixed In composition in the QWRs, no reasonable variation in the QWR width or height would account for a 47 meV variation in the ground state excitonic transition energy. Therefore, we conclude that the energy splitting between P_1 and P_2 and QWR width fluctuations are also accompanied by differences in the In composition between the inner and outer BSL layers.

B. Band filling and nonlinear optical effects in QWRs

Band filling effects in these QWR structures were also examined. In sample 2067, we observed blueshifts in the peak positions of P_1 and P_2 as the excitation density increased. By increasing the probe current, I_b, from 50 pA to 10 nA, components P_1 and P_2 showed a nearly identical shift of ~ 30 meV, as shown in Fig. 4. However, the polarization ratio $I_\parallel/I_\perp$ varies differently for P_1 and P_2 as also shown in Fig. 4. The ratio $I_\parallel/I_\perp$ reduces for P_2 as the probe current increases, but remains nearly constant for P_1. The change of polarization anistropy as a result of band filling has been studied previously with a $\mathbf{k}\cdot\mathbf{p}$ model that takes both 2D quantum confinement and the coherent strain into account, showing important nonlinear optical effects in these samples.[13] Applying this model to these sample structures, we find that the polarization ratio should likewise reduce as the excitation density increases for these samples. The reason for the slower change in the polarization ratio of P_1 is, however, unclear, and may relate to differences in heavy- and light-hole characters between different QWR regions.[13]

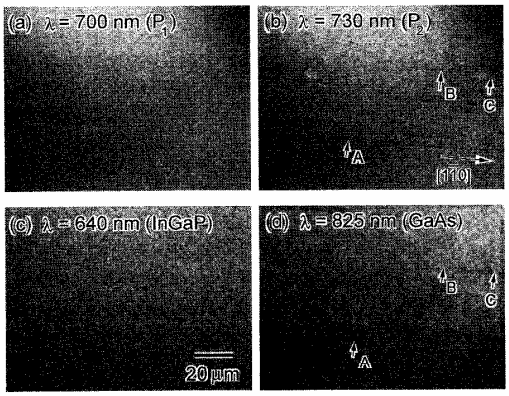

FIG. 5. Monochromatic CL images taken from sample 2067 with wavelength corresponding to BSL luminescence components P_1 (a) and P_2 (b), $In_{0.49}Ga_{0.51}P$ bulk emission (c) and GaAs substrate emission (d).

C. Monochromatic CL imaging of point defects and DLDs

To further investigate the complex origin of the two components in QWR emission, CL images were taken with wavelengths set to the peak wavelength positions for P_1 and P_2, $In_{0.49}Ga_{0.51}P$ bulk, and GaAs substrate emissions, as shown in Fig. 5. An electron beam with energy E_b = 15 keV was used to obtain these CL images for sample 2067. A spotty pattern is observed with spot positions correlating in all four images. This is similar to that observed in MOCVD-grown structures.[12] The spatial correlation among these images indicates that these defects arise from the GaAs substrate or were formed during the initial stages of growth of $In_{0.49}Ga_{0.51}P$ on the GaAs substrate. These defects may form as a result of the agglomeration of In on the GaAs surface, as previously observed during InGaP/GaAs growth.[12] In addition, dark line defects (DLDs) were observed in the images corresponding to the P_2 and GaAs luminescence in Fig. 5. Such DLDs remarkably were not detected in the images for P_1 and $In_{0.49}Ga_{0.51}P$ emission. As discussed above, P_2 dominates the luminescence when the excitation is close to the surface and QWR region 1. The absence of DLDs in the intermediate regions denoted by P_1 and InGaP luminescence (i.e., the 700 and 640 nm images, respectively) is at first glance troubling. However, a close inspection of the 730 and 825 nm images reveals that the DLDs are not directly spatially correlated. Rather, some DLDs appear as finite parallel segments whose positions in the 730 and 825 nm images are displaced along the [1$\bar{1}$0] direction. Consider, for example, positions marked by arrows A, B, and C in these images. Arrows A and C point to DLD segments in the 825 nm image, which are absent in the 730 nm image. The converse is true for the region marked by arrow B, denoting a DLD segment in the 730 nm image. Such a behavior reflects a stepping sequence in the nucleation and propagation of 60° misfit dislocations, and has been observed in InGaAs/GaAs MQWs.[20,21]

In the standard approach to dislocation formation in strained III–V systems,[22] the substrate is considered to have a fixed number of threading dislocation sources and substrate surface defects, which act as heterogeneous nucleation sites for 60° threading dislocations. Once the thickness of the InGaP and $(InP)_2/(GaP)_2$ BSL layers has reached a value where the strain force is equal to the dislocation line tension, the dislocation will glide laterally on a {111} slip plane, resulting in the elongation of the dislocation in an interfacial plane. The length of the misfit segment during growth is controlled by several factors, including frictional forces, impurities, defects, and surface steps, which can effect the eventual pinning of the threading dislocation. A pinned threading dislocation will replicate during growth. Once sufficient strain is attained in the subsequent growth, the dislocation can again elongate on a different layer of the BSL. The current CL data suggests a simple stepping sequence schematically depicted in Fig. 6. Misfit dislocations form at the lower GaAs/InGaP interface, after which the pinned threading segments again elongate into a second misfit dislocation near the top BSL 1 interface. This model explains the segmentation and correlation of the DLD contrast in the 730 and 825 nm images of Fig. 5. To our knowledge, this is the first observation of a dislocation stepping behavior in the InGaP/GaAs system.

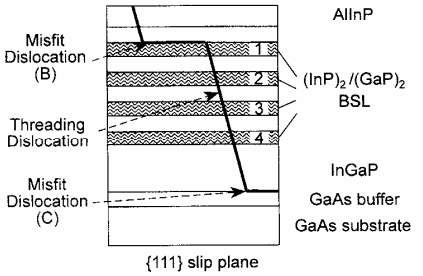

FIG. 6. Schematic showing stepping sequence of 60° dislocations in the BSL structure. In this model, the threading dislocation segments elongate (bend over) into misfit dislocations at the GaAs/InGaP (bottom) and BSL/InGaP (top) interfaces. The diagram shows a {111} slip plane. Misfit dislocation segments B and C correspond to those labeled in Fig. 5.

In sample 2339, the CL images (Fig. 7) showed the characteristic spotty pattern, but no evidence of DLD formation was observed. Also, the variation in line shape with beam energy was substantially reduced compared to the behavior of sample 2067 above. These results strongly suggest that the strain in 2339 is below that necessary to induce the formation of misfit dislocation since the thickness of the BSL in sample 2339 is smaller than that in sample 2067. Therefore, in SILO QWR structures, we demonstrate an apparent relationship between exceeding the critical thickness for misfit dislocation and DLD formation and the presence of multiple components in the QWR luminescence.

D. Time-delay CL measurements of the carrier relaxation, reemission, and diffusion

In order to examine the relaxation and collection of carriers into the QWRs, we have performed a time-resolved CL

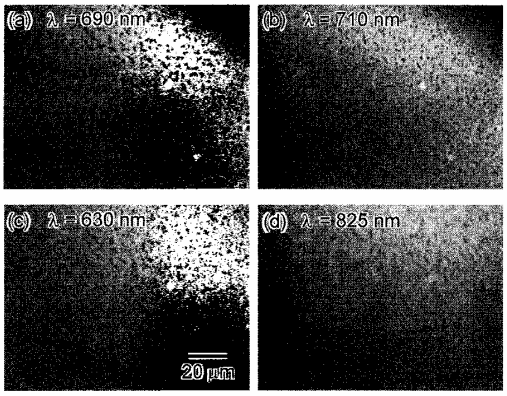

FIG. 7. Monochromatic CL images taken from sample 2339 with wavelength λ=690, 710, 630, and 825 nm, respectively.

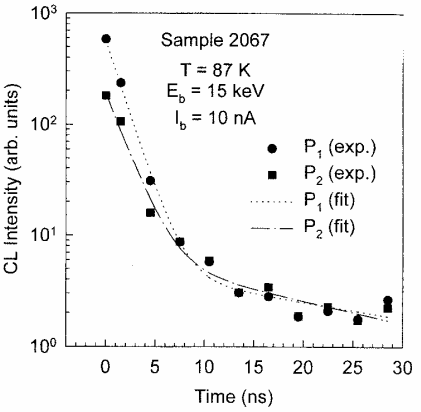

FIG. 9. Intensities of BSL emission components P_1 and P_2 as a function of time. At $t=0$, the electron beam is turned off. Biexponential fits are shown with dotted and dash lines for P_1 and P_2, respectively.

study at $T=87$ K. Shown in Fig. 8 is a stack plot of CL spectra taken from sample 2067 for various time windows with $E_b=15$ keV and $I_b\simeq 10$ nA. During the onset phase (windows O1–O5), a broad feature for $680\lesssim\lambda\lesssim750$ nm is observed with no distinct peaks, indicating a relatively uniform capture into all four QWR regions. A small narrowing and redshifting of the spectra is observed during the progression from the O1 to O6 time windows. The peak labeled *in pulse* represents a measurement in the center of the 50 ns excitation pulse during which a near-steady-state $e-h$ generation and recombination rate has been reached. A rapid narrowing and redshifting is observed during the decay phase, D1–D7 windows in Fig. 8. The CL intensity of the two CL components P_1 and P_2 versus time is obtained by decomposing the time-delayed CL spectra for each time window shown in Fig. 9. The CL intensity decay versus time is shown in Fig. 9, where dot and dash lines represent biexponential fits to the data.[23] The initial decay time constant is 1.6 ns for P_1 and 1.8 ns for P_2. The faster decay rate for P_1 and the reversal of P_1 and P_2 intensities indicate that channels for the diffusive transport of carriers between the P_1 and P_2 levels (QWR regions 4 and 1) exist. This should not be surprising, given that the distance between regions 1 and 4 is ~830 Å, substantially less than the diffusion length of ~0.5 μm. Thermal reemission from the QWR regions before recombination will occur, leading to an eventual carrier transfer into the lowest energy (P_2-like) states for transients exhibiting the longest decay times. The redshift of both P_1 and P_2 during the decay phase is ~30 meV (determined from fits not shown) and this is due to the reduction of quasi-Fermi-level difference as excess carrier density decreases with time. The energy shifts in the time-delayed CL spectra are complimentary to those observed in the excitation-dependent results of Fig. 4(a).

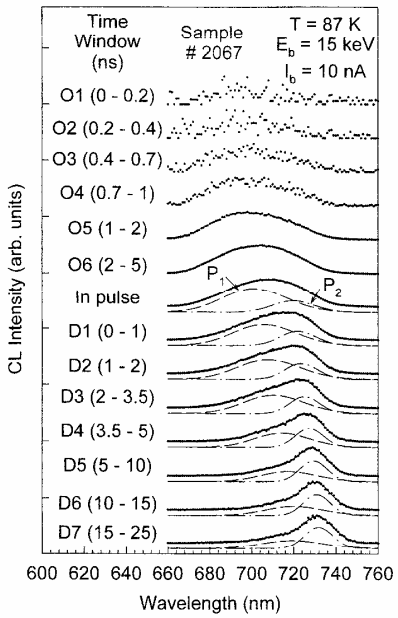

FIG. 8. Stack plot of time-delay CL spectra various onset (O*i*) and decay (D*i*) time windows (for sample 2067). All spectra are renormalized to have about the same maximum peak height.

IV. SUMMARY AND CONCLUSIONS

In conclusion, we have examined the nonlinear optical properties and structural properties using the cathodoluminescence techniques. In comparison to the MOCVD-grown structure previously studied,[12–14] the gas source MBE-grown structures in this study show a higher degree of lateral ordering and narrower QWRs. The narrower QWRs in MBE suggest that surface reaction kinetics and the mass transfer rates play an important role in the lateral diffusion and phase separation of $(InP)_2/(GaP)_2$. Two distinct components, P_1 and P_2, were observed in the sample with the thicker QWR regions. The beam energy dependence of the CL spectral line shape indicated variations in the In composition modulation

and QWR lateral dimensions between the inner and outer $(InP)_2/(GaP)_2$ BSL regions. The outer BSL has a ~6% higher In composition modulation as a result of a strain accumulation effect.[6,9] Strong phase-space filling and nonlinear optical effects were observed for these samples, consistent with the narrowing of the density of states in QWRs.[13] Likewise, a strong excitation dependence of the polarization anisotropy was observed, also consistent with a QWR-like behavior.[13] CL imaging, however, revealed defects in a spotty pattern that are tied to the initial stages of InGaP growth on GaAs. Also, misfit dislocations were found to form for the sample with a thicker BSL region. Monochromatic CL imaging revealed that misfit dislocations and DLDs formed in a stepping sequence with finite segments close to the GaAs/InGaP interface and uppermost BSL layers (BSL region 1). Time-delayed CL spectra were acquired to examine the carrier capture and relaxation dynamics. A uniform capture of carriers into the four QWR regions was observed during the onset time windows. A rapid transfer of carriers between the QWR regions occurs on a sub-ns time scale. This was observed during the decay phase, as carrier reemission, diffusion, and thermalization occurs between inner and outer BSL regions, i.e., over distances of ~0.1 μm. The quantum efficiency of QWR lasers depends on the carrier collection efficiency of the QWRs. Future time-resolved CL studies of these SILO QWRs will focus on the temperature dependence of the carrier relaxation, band filling, and polarization anisotropy in order to optimize the carrier collection in the QWR at room temperature.

ACKNOWLEDGMENTS

This work was supported by the U.S. Army Research Office (Grant Nos. DAAH04-94-G-0260 and DAAH04-95-1-0386), the National Science Foundation (Grant Nos. ECS-94-09122, ECD-89-43166, and DMR-89-2-538), the Joint Services Electronics Program (N00014-96-1-0129), and the Office of Naval Research University Research Initiative Program (N00014-92-J-1519KC).

[1]J. W. Cahn, Acta Metall. **9**, 975 (1961).
[2]G. B. Stringfellow, J. Cryst. Growth **27**, 21 (1974).
[3]P. Henoc, A. Izrael, M. Quillec, and H. Launois, Appl. Phys. Lett. **40**, 963 (1982).
[4]F. Glas, J. Appl. Phys. **62**, 3201 (1987).
[5]A. A. Mbaye, L. G. Ferreira, and A. Zunger, Phys. Rev. Lett. **58**, 49 (1987).
[6]K. C. Hsieh and K. Y. Cheng, Mater. Res. Soc. Symp. Proc. **379**, 145 (1995).
[7]A detailed discussion of the relevance of Refs. 1–5 towards understanding strain-induced lateral ordering in III–V alloys can be found in Ref. 6.
[8]K. C. Hsieh, K. Y. Cheng, Y. L. Hwang, T. Zhang, and R. M. Kolbas, Appl. Phys. Lett. **68**, 1790 (1996).
[9]S. T. Chou, K. Y. Cheng, L. J. Chou, and K. C. Hsieh, J. Appl. Phys. **78**, 6270 (1995); A. C. Chen, A. M. Moy, P. J. Pearah, K. C. Hsieh, and K. Y. Cheng, Appl. Phys. Lett. **62**, 1359 (1993).
[10]P. J. Pearah, A. C. Chen, A. M. Moy, K. C. Hsieh, and K. Y. Cheng, IEEE J. Quantum Electron. **30**, 608 (1994).
[11]A. Mascarenhas, R. G. Alonso, G. S. Horner, S. Froyen, K. C. Hsieh, and K. Y. Cheng, Phys. Rev. B **48**, 4907 (1993).
[12]Y. Tang, K. Rammohan, H. T. Lin, D. H. Rich, P. Colter, and S. M. Vernon, Mater. Res. Soc. Symp. Proc. **379**, 165 (1995).
[13]Y. Tang, H. T. Lin, D. H. Rich, P. Colter, and S. M. Vernon, Phys. Rev. B **53**, R10 501 (1996); D. H. Rich, Y. Tang, and H. T. Lin, J. Appl. Phys. **81**, 6837 (1997).
[14]D. H. Rich and Y. Tang, Appl. Phys. Lett. **69**, 3716 (1996).
[15]E. M. Stellini, K. Y. Cheng, P. J. Pearah, A. C. Chen, A. M. Moy, and K. C. Hsieh, Appl. Phys. Lett. **62**, 458 (1993).
[16]D. Bimberg, H. Munzel, A. Steckenborn, and J. Christen, Phys. Rev. B **31**, 7788 (1985); H. T. Lin, D. H. Rich, A. Konkar, P. Chen, and A. Madhukar, J. Appl. Phys. **81**, 3186 (1997).
[17]We integrate the depth–dose curve $g(z)$ over the first and fourth layers to estimate the ratio of the $e-h$ generation rates, as described in T. E. Everhart and P. H. Hoff, J. Appl. Phys. **42**, 5837 (1971).
[18]M. Prasad, O. E. Martinez, C. S. Menoni, J. J. Rocca, J. L. A. Chilla, M. J. Hafich, and G. Y. Robinson, J. Electron. Mater. **23**, 359 (1994).
[19]K. Rammohan, H. T. Lin, D. H. Rich, and A. Larsson, J. Appl. Phys. **78**, 6687 (1995).
[20]J. Wang, J. W. Steeds, and D. A. Woolf, Philos. Mag. A **65**, 829 (1992).
[21]D. H. Rich, H. T. Lin, Y. Tang, K. Rammohan, and A. Larsson, Scanning Microsc. Suppl. (in press).
[22]J. W. Mathews, A. E. Blakeslee, and S. Mader, Thin Solid Films **33**, 253 (1976).
[23]P. Dua, S. L. Cooper, A. C. Chen, and K. Y. Cheng, Appl. Phys. Lett. **69**, 2261 (1996).